PAPER

Wire-in-tube structure fabricated by single capillary electrospinning *via* nanoscale Kirkendall effect: the case of nickel–zinc ferrite†

Jiecai Fu,‡*[a] Junli Zhang,‡[a] Yong Peng,[a] Changhui Zhao,[a] Yongmin He,[a] Zhenxing Zhang,[a] Xiaojun Pan,[a] Nigel J. Mellors[b] and Erqing Xie*[a]

Wire-in-tube structures have previously been prepared using an electrospinning method by means of tuning hydrolysis/alcoholysis of a precursor solution. Nickel–zinc ferrite ($Ni_{0.5}Zn_{0.5}Fe_2O_4$) nanowire-in-nanotubes have been prepared as a demonstration. The detailed nanoscale characterization, formation process and magnetic properties of $Ni_{0.5}Zn_{0.5}Fe_2O_4$ nanowire-in-nanotubes has been studied comprehensively. The average diameters of the outer tubes and inner wires of $Ni_{0.5}Zn_{0.5}Fe_2O_4$ nanowire-in-nanotubes are around 120 nm and 42 nm, respectively. Each fully calcined individual nanowire-in-nanotube, either the outer-tube or the inner-wire, is composed of $Ni_{0.5}Zn_{0.5}Fe_2O_4$ monocrystallites stacked along the longitudinal direction with random orientation. The process of calcining electrospun polymer composite nanofibres can be viewed as a morphologically template nucleation and precursor diffusion process. This allows the nitrates precursor to diffuse toward the surface of the nanofibres while the oxides (decomposed from hydroxides and nitrates) products diffuse to the core region of the nanofibres; the amorphous nanofibres transforming thereby into crystalline nanowire-in-nanotubes. In addition, the magnetic properties of the $Ni_{0.5}Zn_{0.5}Fe_2O_4$ nanowire-in-nanotubes were also examined. It is believed that this nanowire-in-nanotube (sometimes called core–shell) structure, with its uniform size and well-controlled orientation of the long nanowire-in-nanotubes, is particularly attractive for use in the field of nano-fluidic devices and nano-energy harvesting devices.

Introduction

Nanocables or composite one-dimensional nanostructures with core–shell heterostructures offer a wealth of interesting applications, include nano-catalysis, nano-machinery, sensing, drug delivery, environmental protection and use as building blocks for functional devices.[1–6] Numerous synthetic methods for the formation of such nanocable structures have been developed. For example, radial metal-semiconductor heterostructures (Au–Te) have been obtained by carefully coating one face of the membrane pore with a metal film, thus forming metal nano-tubes, and then further electrodepositing the semiconductors radially inside the metal nanotubes with a slow deposition rate.[7] Silicon carbide and silicon oxide sheathed with boron nitride and carbon have been successfully synthesized by means of reactive laser ablation.[8] Still, the above-described methods

possess some distinct disadvantages, such as high cost and the involvement of a complicated multi-step process. It has thus been difficult to realize any practical industrial production and currently there is a lack of sophisticated nanotechnologies to develop these free-standing nanowire building blocks into functional nano-devices. The ever-increasing applications of nanocables or radially core–shell heterostructures in the new field of bio-medicine and nano-energy demand novel fabrication methods which have a promising potential to realize large-scale production of high quality free-standing nanostructures. The use of electrospinning is believed to offer the possibility to achieve this goal.

There has been rapidly expanding interest in electrospinning during recent years, owing to its many attractive features, such as its comparatively low-cost and relatively high production rate, its ability to generate materials with large surface area-to-volume ratios and its applicability to many types of materials.[9–12] By controlling the electrospinning conditions, various interesting structures with unique properties, including ultrafine nanofibres, beaded nanofibres, porous nanofibres, nanotubes, and nanobelts and three-dimensional architectures, can easily be obtained.[13–18] More interestingly, nanowire-in-nanotubes (WIT, or core–shell structures) can currently be fabricated, which is usually under two different strategies: rapid

[a] *Key Laboratory of Magnetism and Magnetic Materials of Ministry of Education, Lanzhou University, Lanzhou 730000, P. R. China. E-mail: fujc06@gmail.com; xieeq@lzu.edu.cn; Fax: +86 9318912616; Tel: +86 931 8913554*

[b] *Nano Materials Group, School of Computing, Science and Engineering, University of Salford, Greater Manchester M5 4WT, UK*

‡ These authors contributed equally to this work.

annealing or tributyltin (TBT) addition.[19,20] In rapid-annealing, after the electrospun nanofibres are prepared, they are annealed at a high heating rate, such as 100 °C min^{-1}. On the other hand, the TBT addition method will introduce the unnecessary component (TBT), and it always relies on the properties of select materials. It is known that the electrospinning nanofibre morphologies are often dependent on the conflict arising between the phase separation dynamics and the ion diffusion kinetics, which is caused by the Kirkendall effect and determined by the ion type during the calcination process.[21,22] However, the published literature does not take fully into consideration such dynamical advantages, focusing only on post-modification. Moreover, the literature does not converge to a unifying explanation of morphology determination during the electrospinning process.

Recently, Haifan Xiang and Yongliang Cheng *et al.* have contributed a method and mechanism to interpret the formation of hollow nanofibres.[23,24] They reported that the hollow nanofibres can be obtained when the ion (decomposed oxides precursors) diffusion speed dominates the phase separation. A sharp interface develops in the hollow fibre only when the ion diffusion speed rate is relatively high, whereas a solid structure is obtained at a relative low ion diffusion speed. These studies suggest that it is possible to control the calcined structure by adjusting the ion diffusion rate and path. Here, we demonstrate that nanowire-in-nanotubes can be fabricated through electrospinning by intentionally creating partial hydrolysis/alcoholysis with a relatively low ion diffusion speed in the electrospun polymer composite nanofibres. The partial hydrolysis/alcoholysis sol–gel was introduced by using a heating enclosure enclosing the glass syringe in order to increase the temperature of the sol–gel in the glass syringe during the electrospinning process.

$Ni_{0.5}Zn_{0.5}Fe_2O_4$ has been used widely in the field of high frequency devices and giant magnetoelectric resistance owing to its distinctive properties, such as high resistivity value, little eddy current loss in high frequency and excellent chemical stability.[25,26] Studies on the preparation of $Ni_{0.5}Zn_{0.5}Fe_2O_4$ nanostructures have been reported extensively in terms of various well-established techniques and several nanostructures have been fabricated, such as nanoparticles and nanocrystals embedded in thin films.[27,28] However, little research has been reported on $Ni_{0.5}Zn_{0.5}Fe_2O_4$ WIT, which might be very useful in developing new applications for $Ni_{0.5}Zn_{0.5}Fe_2O_4$. For example, in the field of bio-medical applications WIT, in terms of its structural attributes, has great advantages in biological applications owing to its distinctive inner and outer surfaces, in comparison to conventional structures. Inner voids can be used to capture, concentrate and release species ranging in size from large proteins to small molecules because the tube dimensions can easily be controlled by adjusting the experimental parameters. Distinctive outer surfaces can be differentially functionalized with environmentally friendly and/or probe molecules to respond to a specific target. Therefore, by combining the desired tubular structure with magnetic properties, the magnetic nanotube could be an ideal candidate for providing multifunctional nanomaterials in biomedical applications, such as targeting drug delivery with a magnetic resonance imaging capability.

In this project, $Ni_{0.5}Zn_{0.5}Fe_2O_4$ WITs have been fabricated by electrospinning. The detailed nanoscale characterization, growth mechanism and magnetic properties of $Ni_{0.5}Zn_{0.5}Fe_2O_4$ WITs have been comprehensively studied. In addition, a possible mechanism based on the nanoscale Kirkendall effect was proposed to explain the formation of $Ni_{0.5}Zn_{0.5}Fe_2O_4$ WITs. It is believed that this work may suggest a new route for devising the large-scale production of various materials with WIT structures and, in addition, may expand future applications in semiconductor energy harvesting, photo-detection and in the field of bio-medical applications.

Experimental

Synthesis of $Ni_{0.5}Zn_{0.5}Fe_2O_4$ WITs

$Ni_{0.5}Zn_{0.5}Fe_2O_4$ WITs were prepared using an electrospinning technique. In a typical synthesis, 0.25 mmol nickel nitrate hexahydrate ($Ni(NO_3)_2 \cdot 6H_2O$, A.R., Alfa-Aesar Inc., USA), 0.25 mmol zinc nitrate hexahydrate ($Zn(NO_3)_2 \cdot 6H_2O$, A.R., Alfa-Aesar Inc., USA), 1 mmol iron nitrate nonahydrate ($Fe(NO_3)_3 \cdot 9H_2O$, A.R., Alfa-Aesar Inc., USA), and 0.17 g poly vinylpyrrolidone (PVP, $M_w \approx 1\ 300\ 000$, Sigma-Aldrich Inc., USA) were dissolved in a mixed solution of 1.25 mL ethanol (A.R., Tianjin Chemical Corp., China) and 1.25 mL *N,N*-dimethyl formamide (DMF, A.R., Tianjin Chemical Corp., China) under continuous and vigorous stirring by a magnetic stirrer for 4 h. A homogenous PVP/nickel nitrate/iron nitrate/zinc nitrate sol–gel was obtained and then transferred into a dedicated electrospinning setup (Fig. 1a). A special feature of this setup is that a heating accessory was mounted outside the glass syringe to maintain a constant temperature of the sol–gel solution, which ensured a controllable partial hydrolysis (or alcoholysis) of the nitrates. Therefore, the sol–gel precursor was composed of PVP, nitrates, hydroxides (iron hydroxide, nickel hydroxide, zinc hydroxide), ethanol, and DMF. The electrospinning process was performed at 12 kV DC voltage with 15 cm spacing between cathode (a metal collector) and anode (needle), and a feed rate of 0.4 mL h^{-1} pumped by a syringe pump (LSP01-1A, Baoding Longer syringe pump Corp., China). The electrospun polymer composite fibres were collected using an alumina crucible and then dried in a vacuum chamber at 60 °C for 6 h. The nanofibres were subsequently annealed in an air atmosphere at 200 °C with a heating rate of 1 °C min^{-1}, and then sintered at 650 °C for 2 h with a heating rate of 1 °C min^{-1} in an air atmosphere. The sample was eventually cooled down to room temperature with a cooling rate of 2 °C min^{-1}.

Characterization

The morphological, crystal structural and chemical characterization of the electrospun polymer composite nanofibres and calcined $Ni_{0.5}Zn_{0.5}Fe_2O_4$ WITs were analyzed at the nanoscale using a high-resolution transmission electron microscope (HRTEM, Tecnai™ G^2 F30, FEI, USA) equipped with energy-dispersive X-ray spectroscopy (EDAX, AMETEK Co., LTD, USA), high angle annular dark field and scanning transmission electron microscopy (HAADF-STEM), and X-ray diffraction (XRD,
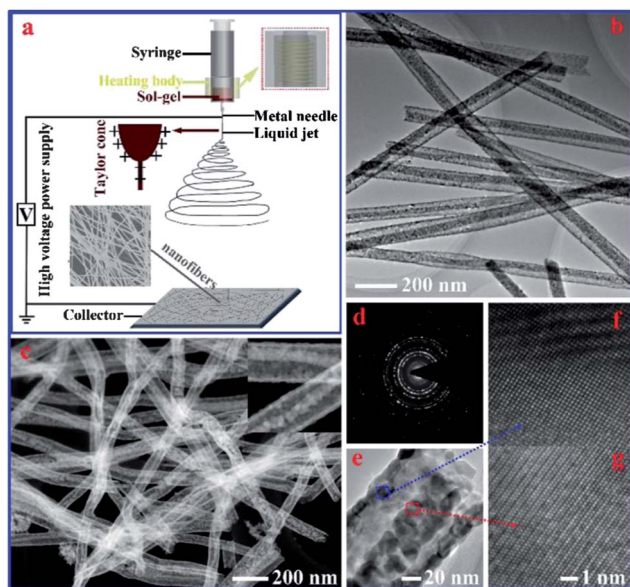
Fig. 1 (a) Schematic illustration of the dedicated electrospinning apparatus for preparing WITs, which consists of four major components: a high voltage power supply; a syringe with a metallic spinneret needle; a grounded collector; and a heated enclosure. A heated circulating water system was used to increase the temperature of the body. Top-left inset shows a drawing of the electrified Taylor cone. The middle-left inset displays a typical SEM image of the electrospun polymer composite nanofibres collected from a metal collector. (b) A representative low-magnified TEM image of $Ni_{0.5}Zn_{0.5}Fe_2O_4$ WITs; (c) low-magnified HAADF-STEM images of individual $Ni_{0.5}Zn_{0.5}Fe_2O_4$ WITs, and inset is a HAADF-STEM image of two crossed $Ni_{0.5}Zn_{0.5}Fe_2O_4$ WITs; (d) SAED pattern of the WITs in (b); (e) a highly magnified TEM image showing the detailed structure of WIT; (f) and (g) lattice fringe images corresponding to the nanoparticles made up of WIT in the TEM image (marked by blue and red squares).

Philips X'pert Pro MPD, Netherlands). The transformation of the precursor nanofibres into $Ni_{0.5}Zn_{0.5}Fe_2O_4$ WITs was investigated by a commercial thermogravimetry/differential thermal analysis apparatus (TG-DTA, Diamond, USA) with a heating rate of $1\,^{\circ}C\ min^{-1}$. The magnetic properties of $Ni_{0.5}Zn_{0.5}Fe_2O_4$ WITs were measured by a superconducting quantum interference device (SQUID, MPMS-XL, Quantum design, UK).

Results and discussions

$Ni_{0.5}Zn_{0.5}Fe_2O_4$ WITs morphology and structure

Fig. 1b shows a representative TEM image of calcined $Ni_{0.5}Zn_{0.5}Fe_2O_4$ nanofibres. A continuous structure and virtually uniform diameter can be seen in each nanofibre after the PVP was removed by the calcination process. The tubular structure with one wire inside can be seen clearly. EDX spectrum and mappings (see ESI Fig. S1† for details) of a single $Ni_{0.5}Zn_{0.5}Fe_2O_4$ nanofibre indicates the elements O, Ni, Zn and Fe are evenly distributed throughout the whole nanofibre, revealing a uniform chemical phase. The quantitative analysis shows that the average diameter of the outer nanotubes is about 120 nm (ranging from 100 nm to 130 nm), whilst that of the inner nanowires is approximately 42 nm, ranging from 35 nm to 50 nm.

In order to observe the morphology of the $Ni_{0.5}Zn_{0.5}Fe_2O_4$ nanofibres better, the HAADF-STEM technique was adopted. In comparison to the bright field TEM, the contrast of incoherent high-resolution HAADF-STEM images depends directly on the sample atomic number Z and the thickness of the materials.[9] HAADF-STEM also has a much better spatial resolution because of a better depth of field, which makes it very useful in observing the spatial shape of nanomaterials. Fig. 1c shows a representative HAADF-STEM image of the $Ni_{0.5}Zn_{0.5}Fe_2O_4$ nanofibres, revealing a much clearer image of the tubular structure with one wire inside. A high-magnification HAADF-STEM image (inset of Fig. 1c) clearly shows that the inner wire sticks onto the inner wall of the outer tube of each nanofibre, seeming to act as a support for the outer tube. Therefore, the nanofibres are named $Ni_{0.5}Zn_{0.5}Fe_2O_4$ wire-in-tube nanofibres (WITs) in this work. The WIT structure should have a much better mechanical hardness in comparison with a purely tubular nanofibre because of the support of the inner nanowire. Both the outer tubes and inner wires consist of individual $Ni_{0.5}Zn_{0.5}Fe_2O_4$ nanoparticles, of which the sizes are uniform. The particles are bonded together one-by-one to form a one-particle-thick tube. It is also seen that individual WITs have a continuous and well-defined structure, consistent with the above HRTEM observation. Quantitative analysis shows that the particle size measured is on average 17 nm, and ranges from 12 nm to 24 nm. The diameter of the outer walls of the $Ni_{0.5}Zn_{0.5}Fe_2O_4$ WITs is the same as the above quantitative analysis of bright-field TEM images.

The crystalline structure of the $Ni_{0.5}Zn_{0.5}Fe_2O_4$ WITs was characterized in detail by HRTEM and selected-area electron diffraction (SAED). Fig. 1d shows a representative SAED pattern of a single $Ni_{0.5}Zn_{0.5}Fe_2O_4$ WIT taken from the area in Fig. 1b, which indicates a face-centred cubic polycrystalline structure. Fig. 1f shows a lattice-resolution HRTEM of the single nanoparticle marked by the blue square in Fig. 1e which belongs to the outer tube of the $Ni_{0.5}Zn_{0.5}Fe_2O_4$ WIT, whilst Fig. 1g comes from the nanoparticle of the inner wire marked by the red square. Both HRTEM images reveal a single-crystalline structure. The interplanar spacings were measured to be 2.41 Å (Fig. 1f) and 2.52 Å (Fig. 1g), respectively, which match well with the (222) and (113) planes of cubic $Ni_{0.5}Zn_{0.5}Fe_2O_4$. Further experiments show that the different nanoparticles (either from the outer nanotubes or from inner nanowires) on the same $Ni_{0.5}Zn_{0.5}Fe_2O_4$ WIT have various crystallographic orientations. These results prove that the crystal orientations of individual $Ni_{0.5}Zn_{0.5}Fe_2O_4$ nanoparticles on a $Ni_{0.5}Zn_{0.5}Fe_2O_4$ WIT are arranged randomly.

Formation mechanism of the $Ni_{0.5}Zn_{0.5}Fe_2O_4$ WITs

To understand the formation mechanism of the $Ni_{0.5}Zn_{0.5}Fe_2O_4$ WITs, the morphologies of the precursor nanofibres calcined at five temperature stages (room temperature, 200 °C, 300 °C, 450 °C and 650 °C) were observed by TEM (Fig. 2), which provides a direct insight into the WIT structural evolution during the calcination. Fig. 2a and its inset show the electrospun nanofibres before calcination, revealing a smooth surface. When the
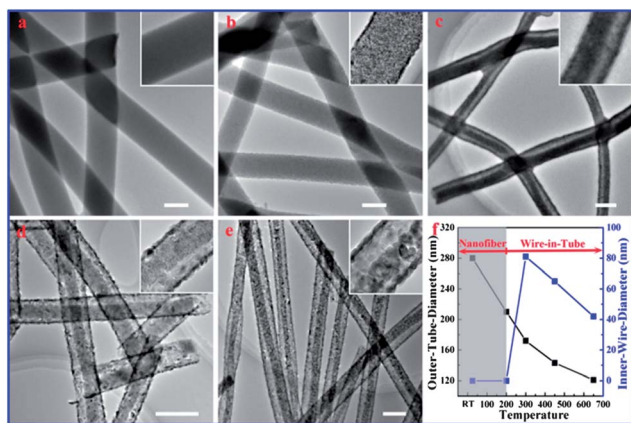
Fig. 2 TEM images showing the morphology evolutions of the successive processes occurring during electrospun polymer composite nanofibre calcination at five different temperature stages and the insets showing the enlarged view of single nanofibres: (a) room temperature; (b) 200 °C; (c) 300 °C; (d) 450 °C; (e) 650 °C. (f) The relationship between calcination temperature and the average diameters (outer-tube-diameter and inner-wire-diameter). All the scale bars are 200 nm.

temperature rises to 200 °C (Fig. 2b), the morphology of the $Ni_{0.5}Zn_{0.5}Fe_2O_4$ WITs does not show any obvious change apart from a smaller diameter. However, the highly magnified TEM image, as shown in the inset of Fig. 2b, shows that their surfaces are not smooth any more. Tiny particle-like structures on each nanofibre were formed, indicating that the precursor nano-fibres start to crystallize with the decomposition of metal nitrates (iron nitrate, nickel nitrate and zinc nitrate) as precursors to metal oxides (confirmed by TG-DTA and XRD measurement, see ESI Fig. S2 and S3† for details). After annealing at 300 °C, the contrast of the TEM image shown in Fig. 2c clearly reveals that the WIT structures have been formed. The tiny particles have grown bigger than the size shown in Fig. 2b. Fig. 2d shows a TEM image of the nanofibres calcined at 450 °C, revealing a much larger grain and rougher surface than the 300 °C fibres in Fig. 2c. The highly magnified TEM image (inset of Fig. 2d) reveals that the nanoparticles in the outer tube were well crystallized, but not the nanoparticles in the inner wire. The final calcination at 650 °C for 2 h caused all inter-mediate products and the polymer residues to be removed, as proved by the TG-DTA and XRD measurement shown in ESI Fig. S2 and S3.† As is clearly seen in the inset of Fig. 2e, the $Ni_{0.5}Zn_{0.5}Fe_2O_4$ WITs, in both the outer-tube and the inner-wire, are composed of individual $Ni_{0.5}Zn_{0.5}Fe_2O_4$ nanocrystallites accumulated along the longitudinal direction. The changes in the average inner and outer diameters of the nanofibres calcined at five temperature stages were measured as shown in Fig. 2f, which provides quantitative evidence of the structural evolution of the $Ni_{0.5}Zn_{0.5}Fe_2O_4$ WITs. With the calcination temperature increasing, the outer-tube-diameter of the nano-fibres always shrinks due to the evaporation of solvent at the relative lower temperature (lower than 200 °C), decomposition of metal nitrates, crystalline growth and burning out of PVP. Before the appearance of an inner-wire, the diameter of the inner-wire was regarded as zero. With the metal (Ni, Zn, Fe)

oxides (decomposed from the corresponding hydroxides) diffusing to the core region of nanofibres gradually, the inner-wire-diameter increases. With further temperature increases, the crystallite in inner-wire growth, along with the cost of merging the relative smaller crystallite and the formation of Ni–Zn ferrite phase, make the structure of inner-wire much denser, as a result, the inner-wire diameter decreases. The chemical reactions and phase transformations of the $Ni_{0.5}Zn_{0.5}Fe_2O_4$ WITs were also verified by TG-DTA and XRD (see ESI Fig. S2 and S3† for details).

Based on the aforementioned experiments and observations, a possible formation mechanism of $Ni_{0.5}Zn_{0.5}Fe_2O_4$ WITs in this work is proposed, of which schematic diagrams are shown in Fig. 3. The formation started from a sol–gel solution composed of PVP, nitrates, hydroxides (iron hydroxide, nickel hydroxide, zinc hydroxide), ethanol, and DMF. During the electrospinning process, once the fibres were spun out from the spinneret, the solvent (especially for ethanol) will evaporate at a relatively faster rate from the nanofibres at the surface compared to that of the centred region, and then a concentration gradient of solvent would form along the radius direction of the fibres. The solvent concentration at the centre of the fibres is higher than that near the surface, and this type of concentration gradient would eventually push the system into an unstable phase state. The nitrates and hydroxides would separate out gradually from the surface to the core-region under the action of the concen-tration gradient of the solvent. It seems that the nitrates- and hydroxides-rich surface will form when the electrospun nano-fibres are loaded on the metal collector. However, the formation of a nitrates-rich surface rather than a hydroxides-rich surface is due to two aspects. One aspect is the low content of hydroxides
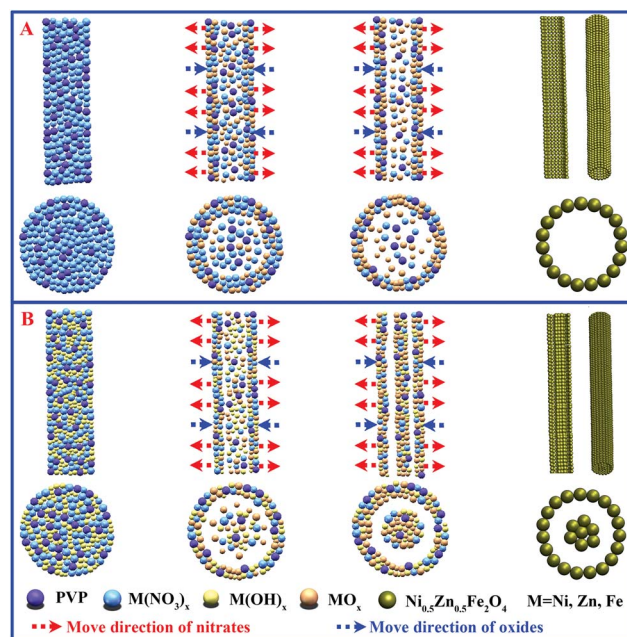

Fig. 3 (A) Schematic diagram of the formation mechanism of $Ni_{0.5}Zn_{0.5}Fe_2O_4$ nanotubes; (B) schematic diagram of the formation mechanism of $Ni_{0.5}Zn_{0.5}Fe_2O_4$ WITs.

at each nanofibre, and the solvent concentration gradient makes almost no effect on the diffusion of hydroxides. Another aspect is the intrinsic difference of nitrate and hydroxides. At the same conditions, the diffusion rate of nitrates is much higher than that of hydroxides (this phenomenon is also the key point of Kirkendall effect reported in previous literature), which makes the formation of a hydroxides-rich surface almost impossible. The nitrates-rich surface of nanofibres is believed to act as an initial template in the later process during the formation of nanotubes. When the calcination temperature reaches or is a little higher than the decomposition temperature of the metal nitrates (~250 °C in this work), the nitrates-rich layers on the surfaces of individual precursor nanofibres decompose into oxide (nickel oxide, zinc oxide and iron oxide) nanoparticles due to the rich presence of oxygen near the surface of the nanofibres. In addition, it promotes the increase of the nitrates concentration gradient from the core to the surface of the nanofibres, which makes most of the nitrates in the core of the nanofibres diffuse to the fibre surface and decompose into oxides, eventually forming the outer nanotube structure. It is noteworthy that the Ostwald ripening effect also plays an important role during the growth of decomposed oxides nanocrystalline at this stage, which has been reported in the literature.[29] Meanwhile, the oxides concentration gradient from the surface to the core of nanofibres also appears. According to the diffusion principle, the oxides would diffuse toward to the core region. However, the diffusion speed of oxides (T_m > 1500 °C) is much slower than that of nitrates (T_m < 500 °C) due to the Kirkendall effect, which makes it impossible for the oxides to diffuse to the core region in large quantities. The designed strategy in our work, hydrolysis/alcoholysis of nitrates introduced by the heating accessory to generate a small amount of hydroxides in the nanofibres, allows the concentration to can be controlled by the additional heating accessory. The decomposed oxides (hydroxides decomposing into corresponding oxides at this temperature range) were dispersed uniformly in the nanofibres. Due to the short diffusion path, those factors' co-action eventually makes the formation of the inner wire structure possible. Until the metallic salt, hydroxides and polymer have been fully exhausted, $Ni_{0.5}Zn_{0.5}Fe_2O_4$ wire-in-tube structures (Fig. 3B) continue to be formed. More experiments prove that larger diameters of inner nanowires were formed when the hydrolysis-/alcoholysis-degree of nitrates in the precursor sol–gel had been increased (for a detailed description see ESI Fig. S4†). In comparison with the traditional formation of electrospun nanotubes (as illustrated in Fig. 3A), the reason for the formation of the wire-in-tube structure has its origins in the existence of the hydroxides.

Magnetic properties of $Ni_{0.5}Zn_{0.5}Fe_2O_4$ WITs

The magnetic properties of the $Ni_{0.5}Zn_{0.5}Fe_2O_4$ WITs were surveyed by SQUID magnetometry. Fig. 4a shows representative magnetic hysteresis loops of the $Ni_{0.5}Zn_{0.5}Fe_2O_4$ WITs measured at four different temperatures (2 K, 50 K, 100 K, and 300 K) in an applied field sweeping from −20 to 20 kOe. The inset shows the hysteresis loops at low magnetic field range to
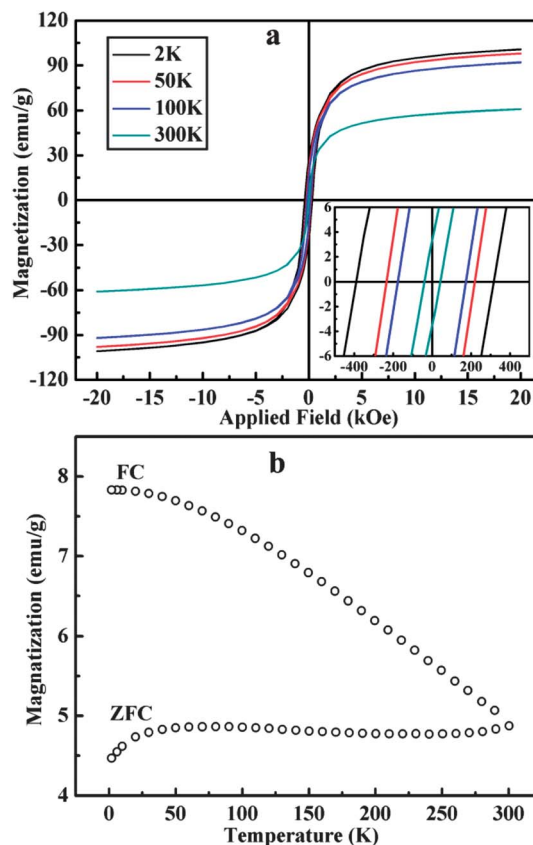
Fig. 4 (a) Hysteresis loops of $Ni_{0.5}Zn_{0.5}Fe_2O_4$ WITs measured at 2 K, 50 K, 100 K and 300 K. Inset shows the hysteresis loops at low magnetic field range; (b) ZFC and FC curves of the $Ni_{0.5}Zn_{0.5}Fe_2O_4$ WITs measured at temperatures ranging from 5 K to 300 K with an applied magnetic field of 50 Oe from SQUID measurements.

demonstrate the coercivity force. The detailed values of the coercivity force (H_c), saturation magnetizations (M_s), and remnant magnetization (M_r) of $Ni_{0.5}Zn_{0.5}Fe_2O_4$ WITs plotted in Fig. 4a are summarized in Table 1. It is found that the $Ni_{0.5}Zn_{0.5}Fe_2O_4$ WITs reveal a typical ferromagnetic behavior and the hysteresis properties observed are strongly dependent on the temperature. The coercivity force of the $Ni_{0.5}Zn_{0.5}Fe_2O_4$ WITs decreases with the increase of temperature, from 317 Oe at 2 K to 43 Oe at 300 K; these values are much larger than those obtained in a previous study for spherical nanoparticles and nanocrystal-embedded thin films.[25,26] It is believed that the large coercivity force derives from the particular WITs' special morphology. As demonstrated in our previous works and others,[9,30,31] a system containing magnetic dipoles arranged in a

Table 1 Magnetic properties of $Ni_{0.5}Zn_{0.5}Fe_2O_4$ WITs measured at different temperatures

Temperature	H_c/Oe	M_s/emu g^{-1}	M_r/emu g^{-1}
2 K	317	101	27.0
50 K	218	98	20.3
100 K	174	92	15.6
300 K	43	61	3.0

linear chain will exhibit an increase in coercivity force. In this work, the $Ni_{0.5}Zn_{0.5}Fe_2O_4$ nanoparticles contained in each WIT (either the inner-wires or the outer-tubes) were also aligned along its length, as in the above TEM observation. Therefore, the dipole–dipole interactions between nanoparticles should tend to align all magnetic dipoles along the WITs' longitudinal axis, which leads to the larger coercivity force. The 43 Oe reading of coercivity at 300 K indicates that the Curie temperature (T_c) of the $Ni_{0.5}Zn_{0.5}Fe_2O_4$ WITs is above the room temperature. The M_s versus temperature also displays a decreasing trend between 101 emu g^{-1} at 2 K and 61 emu g^{-1} at 300 K. However, the decreasing trend is slower than that of the H_c–T curve when the temperature increases from 2 K to 300 K. The saturation magnetization (M_s) of the $Ni_{0.5}Zn_{0.5}Fe_2O_4$ WITs at room temperature (61 emu g^{-1}) is larger than that of bulk nickel-zinc ferrite (57 emu g^{-1}). It is deduced that this derives from the spun-glass-like layer on the surface of the $Ni_{0.5}Zn_{0.5}Fe_2O_4$ WITs.[32]

Fig. 4b shows zero-field-cooled (ZFC) and field-cooled (FC) curves of the $Ni_{0.5}Zn_{0.5}Fe_2O_4$ WITs measured at temperatures ranging from 2 K to 300 K with an applied magnetic field of 50 Oe. In the ZFC measurements, the sample was cooled down to 2 K from room temperature (RT) without the application of an external magnetic field and then heated under an applied magnetic field of 50 Oe while the net magnetization of the sample was recorded. It is observed that there is a large thermal irreversibility and wide energy-barrier distribution in this ZFC curve. This phenomenon could be explained as follows. At the beginning of a ZFC experiment, the magnetic moment of each atom was randomly frozen to an easy axis of a particle. Because the particles contained in the $Ni_{0.5}Zn_{0.5}Fe_2O_4$ WITs were randomly aligned, the net magnetization was small when the field was applied initially. As the temperature increased, the thermal energy freed the spins from the alignment along the easy axis of the $Ni_{0.5}Zn_{0.5}Fe_2O_4$ WITs and allowed the magnetic moments to align with the external applied field. As a consequence, the magnetization exhibited an increasing trend with the increase of temperature. When all the magnetic moments aligned with the external applied field, the magnetization became a constant.

The FC curves were measured by cooling the $Ni_{0.5}Zn_{0.5}Fe_2O_4$ WIT samples under an applied magnetic field of 50 Oe after the ZFC measurement and the FC data provide information about coupling between magnetic moments. The FC magnetization shows a marked decreasing trend with the increase of temperature, indicating a weak dipolar magnetostatic interaction between individual magnetic moments of magnetization. As the temperature decreased the thermal fluctuations also decreased and the magnetic moments of the $Ni_{0.5}Zn_{0.5}Fe_2O_4$ WITs were more easily aligned with the direction of the external applied field. As a result, the $Ni_{0.5}Zn_{0.5}Fe_2O_4$ WITs' magnetization showed a rise in the FC data.

Conclusions

In conclusion, we have demonstrated that WITs with uniform diameters (outer-tube diameter and inner-wire diameter) could be directly fabricated by electrospinning tuned hydrolysis/alcoholysis of the precursor solutions, followed by a calcination process based on the nanoscale Kirkendall effect. The capability and feasibility of this technique have been demonstrated by the fabrication of $Ni_{0.5}Zn_{0.5}Fe_2O_4$ WITs. Each fully calcined individual WIT, either the outer-tube or inner-wire, is composed of $Ni_{0.5}Zn_{0.5}Fe_2O_4$ monocrystallites stacked along the longitudinal direction with random orientation. Detailed nanoscale characterization and formation process investigations reveal that the formation of $Ni_{0.5}Zn_{0.5}Fe_2O_4$ WITs mainly involves morphological template nucleation and precursor diffusion, and a formation mechanism is then proposed based on the Kirkendall effect. It is believed that the method described here will be extendible to many other materials with potential applications in catalysis, energy-harvesting, sensing, encapsulation and drug delivery. The magnetic property studies of $Ni_{0.5}Zn_{0.5}Fe_2O_4$ WITs have demonstrated that dipole–dipole interactions between the nanoparticles contained in the WIT play a dominant role in the magnetization process, which result in the larger coercivity force and saturation magnetization. This new structural form of WIT is expected to have applications in the fields of biomagnetic nano-ferrofluid, magnetic separation, magnetic sensors, etc.

Notes and references

1 S. H. Joo, J. Y. Park, C.-K. Tsung, Y. Yamada, P. Yang and G. A. Somorjai, *Nat. Mater.*, 2008, **8**, 126–131.

2 Y. Qin, X. Wang and Z. L. Wang, *Nature*, 2008, **451**, 809–813.

3 H. Ow, D. R. Larson, M. Srivastava, B. A. Baird, W. W. Webb and U. Wiesner, *Nano Lett.*, 2005, **5**, 113–117.

4 R. Haag, *Angew. Chem., Int. Ed.*, 2004, **43**, 278–282.

5 M. Park, S. Seo, I. S. Lee and J. H. Jung, *Chem. Commun.*, 2010, **46**, 4478–4480.

6 O. Hayden, A. B. Greytak and D. C. Bell, *Adv. Mater.*, 2005, **17**, 701–704.

7 J.-R. Ku, R. Vidu, R. Talroze and P. Stroeve, *J. Am. Chem. Soc.*, 2004, **126**, 15022–15023.

8 Y. Zhang, K. Suenaga, C. Colliex and S. Iijima, *Science*, 1998, **281**, 973–975.

9 J. Zhang, J. Fu, F. Li, E. Xie, D. Xue, N. J. Mellors and Y. Peng, *ACS Nano*, 2012, **6**, 2273–2280.

10 D. Li and Y. Xia, *Adv. Mater.*, 2004, **16**, 1151–1170.

11 J. Fu, J. Zhang, Y. Peng, J. Zhao, G. Tan, N. J. Mellors, E. Xie and W. Han, *Nanoscale*, 2012, **4**, 3932–3936.

12 A. Greiner and J. H. Wendorff, *Angew. Chem., Int. Ed.*, 2007, **46**, 5670–5703.

13 S. H. Tan, R. Inai, M. Kotaki and S. Ramakrishna, *Polymer*, 2005, **46**, 6128–6134.

14 H. Fong, I. Chun and D. H. Reneker, *Polymer*, 1999, **40**, 4585–4592.

15 Y. Z. Zhang, Y. Feng, Z. M. Huang, S. Ramakrishna and C. T. Lim, *Nanotechnology*, 2006, **17**, 901–908.

16 X. H. Li, C. L. Shao and Y. C. Liu, *Langmuir*, 2007, **23**, 10920–10923.

17 E. Q. Xie, Y. R. Su, B. A. Lu, Y. Z. Xie, Z. W. Ma, L. X. Liu, H. T. Zhao, J. Zhang, H. G. Duan, H. L. Zhang, J. Li and Y. Q. Xiong, *Nanotechnology*, 2011, **22**, 285609.

18 J. A. Matthews, G. E. Wnek, D. G. Simpson and G. L. Bowlin, *Biomacromolecules*, 2002, **3**, 232–238.

19 F. Mou, J.-g. Guan, W. Shi, Z. Sun and S. Wang, *Langmuir*, 2010, **26**, 15580–15585.

20 L. Lang, D. Wu and Z. Xu, *Chem.–Eur. J.*, 2012, **18**, 10661–10668.

21 P. Dayal and T. Kyu, *J. Appl. Phys.*, 2006, **100**, 043512.

22 H. Jin fan, M. Knez, R. Scholz, K. Nielsch, E. Pippel, D. Hesse, M. Zacharias and U. Gosele, *Nat. Mater.*, 2006, **5**, 627–631.

23 H. Xiang, Y. Long, X. Yu, X. Zhang, N. Zhao and J. Xu, *CrystEngComm*, 2011, **13**, 4856–4860.

24 Y. Cheng, B. Zou, C. Wang, Y. Liu, X. Fan, L. Zhu, Y. Wang, H. Ma and X. Cao, *CrystEngComm*, 2011, **13**, 2863–2870.

25 A. Verma, T. C. Goel, R. G. Mendiratta and P. Kishan, *J. Magn. Magn. Mater.*, 2000, **208**, 13–19.

26 N. Gupta, A. Verma, S. C. Kashyap and D. C. Dube, *J. Magn. Magn. Mater.*, 2007, **308**, 137–142.

27 S. A. Morrison, C. L. Cahill, E. E. Carpenter, S. Calvin, R. Swaminathan, M. E. McHenry and V. G. Harris, *J. Appl. Phys.*, 2004, **95**, 6392–6395.

28 G. Caruntu, G. G. Bush and C. J. O'Connor, *J. Mater. Chem.*, 2004, **14**, 2753–2759.

29 F.-z. Mou, J.-g. Guan, Z.-g. Sun, X.-a. Fan and G.-x. Tong, *J. Solid State Chem.*, 2010, **183**, 736–743.

30 J. Zhang, J. Fu, G. Tan, F. Li, C. Luo, J. Zhao, E. Xie, D. Xue, H. Zhang, N. J. Mellors and Y. Peng, *Nanoscale*, 2012, **4**, 2754–2759.

31 I. S. Jacobs and C. P. Bean, *Phys. Rev.*, 1955, **100**, 1060.

32 Q. A. Pankhurst and R. J. Pollard, *Phys. Rev. Lett.*, 1991, **67**, 248–250.